Research Square

Preprints are preliminary reports that have not undergone peer review.
They should not be considered conclusive, used to inform clinical practice,
or referenced by the media as validated information.

Moving Without Making Progress: Shorter Forward Runs Explain the Loss of Net Advance in a Model of Swedish Mutant Amyloid Precursor Protein Transport

Andrey V. Kuznetsov

avkuznet@ncsu.edu

North Carolina State University https://orcid.org/0000-0002-2692-6907

Research Article

Keywords: axonal transport, amyloid precursor protein, Alzheimer's disease, stochastic model, Markov chain, observation model, advection–reaction model

Posted Date: November 17th, 2026

DOI: https://doi.org/10.21203/rs.3.rs-11731373/v1

License: This work is licensed under a Creative Commons Attribution 4.0 International License.
Read Full License

Additional Declarations: The authors declare no competing interests.

Moving Without Making Progress: Shorter Forward Runs Explain the Loss of Net Advance in a Model of Swedish Mutant Amyloid Precursor Protein Transport

Andrey V. Kuznetsov

Department of Mechanical and Aerospace Engineering, North Carolina State University, Raleigh, NC 27695-7910; e-mail: avkuznet@ncsu.edu

Abstract

Amyloid precursor protein (APP) reaches axons by fast anterograde transport, and its Swedish mutation causes familial Alzheimer's disease. Two published observations of this mutant in human stem cell–derived neurons seem to conflict. In 30-s movies, most Swedish APP vesicles remained stationary. Yet in fixed axons, 100–200 μm from the soma, the fluorescence of tagged Swedish APP reached 79% of the wild-type signal after normalization to soma intensity. To test whether the tracked vesicles could sustain this signal, we fitted a five-state transport model to the trajectory statistics and combined the fitted kinetics with APP turnover to predict cargo density along the axon. The fitted mean anterograde run shortened from 4.42 μm for wild-type APP to 0.39 μm for Swedish APP, close to the 0.30-μm retrograde runs, so retrograde runs undid nearly all forward progress. With the same 3.63-h half-life for both variants, these kinetics predicted a distal Swedish signal only 6% of the wild-type signal, far below the observed 79%. Vesicle transport alone therefore cannot account for the distal signal. Adding a second, longer-range component, possibly a tagged cleavage product or a second carrier population, reproduced both profiles and predicted a separate wild-type control without refitting. The comparison assumes that kinetics measured during expression of one APP variant apply when both variants are co-expressed. Lysosome recordings tested whether Swedish APP sequesters retrograde motors, leaving fewer for other cargoes. In the fits, retrograde lysosome runs began more often with Swedish APP but ended sooner, which argues against sequestration from a fixed pool of activated motors. Counting directional particle crossings and particle density in the same axonal segment would establish how much vesicle flux accompanies the distal fluorescence.

Keywords: axonal transport, amyloid precursor protein, Alzheimer's disease, stochastic model, Markov chain, observation model, advection–reaction model

1 Introduction

At 100–200 μm from the cell body, images of fixed human axons show a substantial signal from fluorescently tagged Swedish mutant amyloid precursor protein (APP). What carried the label there? Fast anterograde transport, directed away from the cell body, normally carries APP along axons [1,2], and impaired transport can precede amyloid deposition in mouse models of Alzheimer's disease [3,4]. Yet fast movement does not guarantee net progress. A vesicle that runs forward and then backward covers the same stretch of axon twice and ends where it started. For cargoes that alternate between anterograde runs driven by kinesin motors, retrograde runs (toward the cell body) driven by dynein motors, and pauses [5-7], net advance depends on the distances covered in each direction and the time spent moving or paused.

The Swedish double mutation (KM670/671NL) complicates the question because it also changes what a fluorescent tag can report. The mutation lies next to the β-secretase cleavage site and increases amyloidogenic processing [8,9], so a tag may mark a cleavage fragment as well as intact APP. The mutation also changes transport. In 30-s movies of neurons derived from human neural stem cells, 78% of the tracked Swedish APP particles were stationary. The recorded trajectory of one particle is called a track. Among the tracks that moved, forward and backward motion took up equal fractions of the recording [10]. We refer to that work below as the source study. Enhanced β-secretase processing had already been linked to impaired anterograde transport in mouse neurons [11]. The human data allow a more quantitative question. After accounting for pauses, reversals, and turnover (the loss of APP by degradation or cleavage), could the vesicles in the movies sustain the fluorescence seen in fixed axons?

We used stochastic and continuum descriptions of axonal transport [12-15] to predict the fluorescence profiles in fixed cells from rates fitted to the 30-s movies. This gave the images a specific role. They could test whether the tracked vesicles accounted for the signal and, if not, constrain the spatial range of an additional source. The accompanying recordings of early endosomes, identified by the small GTPase Rab5 and referred to below as Rab5, and of lysosomes [10] offered a separate test. If Swedish APP leaves fewer activated retrograde motors available for other cargoes, those cargoes should start retrograde runs less often.

2 Methods

2.1 How a sequence of runs produces drift

We represent a vesicle's position along the axon by x, with the soma at $x = 0$. A vesicle switches at random among five states. It can run anterogradely, away from the soma (A, velocity $+v_a$), or retrogradely, toward the soma (R, velocity $-v_r$). Three further states distinguish brief pauses (P), intermediate arrest (D, termed the detached state), and long-lived immobilization (S, termed the stationary

state). These three states have zero velocity. The names are labels for behavior over time. The trajectories alone do not establish the biochemical nature of each state. Because D and S differ only in how long a vesicle stays immobile, the data may not distinguish all three immobile states. We refitted the model with three and four states to test how many the observations support (Sec. 2.3 and Appendix). The allowed transitions are A ⇄ P, R ⇄ P, P ⇄ D, and D ⇄ S (Fig. 1), so a vesicle must pause before it reverses. We call the chain closed when vesicles are neither added nor lost. Because the transition diagram has no loops (it forms a tree), the steady-state occupancies of the closed chain, π_i (the fraction of time a vesicle would spend in state i over a long observation), satisfy the detailed balance relations below, where k_{ij} is the rate of transition from state i to state j.

$$\pi_A/\pi_P = k_{pa}/k_{ap} \tag{1a}$$

$$\pi_R/\pi_P = k_{pr}/k_{rp} \tag{1b}$$

$$\pi_D/\pi_P = k_{pd}/k_{dp} \tag{1c}$$

$$\pi_S/\pi_D = k_{ds}/k_{sd} \tag{1d}$$

Two speeds, four independent occupancies (the five sum to one), and four forward rates (k_{ap}, k_{rp}, k_{pd}, k_{ds}) specify the model. Equations (1a)–(1d) then set the four reverse rates. Weighting each run velocity by its occupancy gives the mean signed velocity, or drift, of the closed chain in Eq. (2).

$$v_{eff} = v_a\pi_A - v_r\pi_R \tag{2}$$

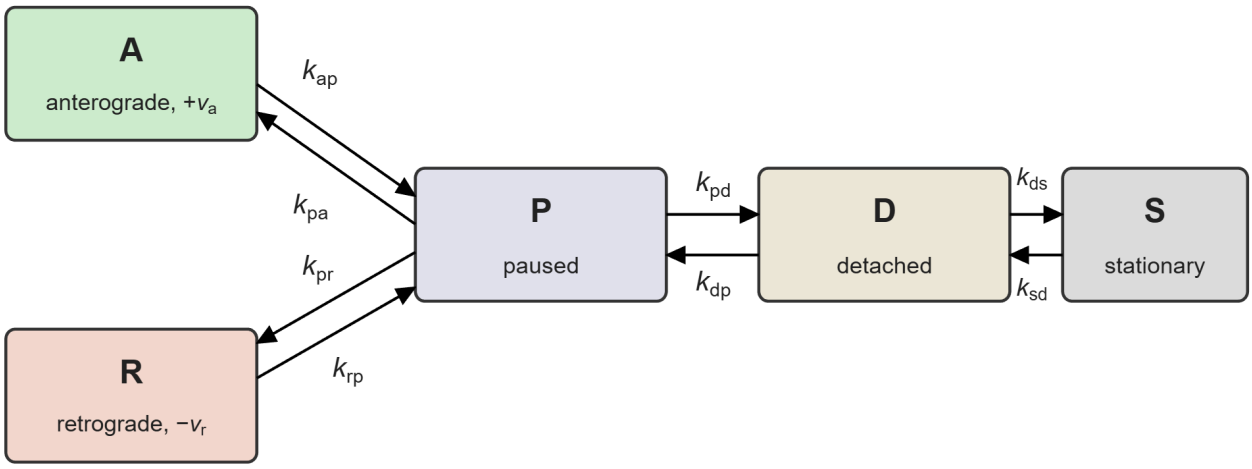


Fig. 1 Five-state model of cargo transport. A and R are motile states with speeds v_a and v_r; P, D, and S are immobile states with increasing residence times. Reversals pass through P, and the transitions form a tree, so that detailed balance fixes k_{pa}, k_{pr}, k_{dp}, and k_{sd} given the occupancies and the four forward rates.

2.2 Reproducing the selection of tracks and frames

The published summaries are of two kinds. Some classify entire tracks, and others describe individual frames within the subset of moving tracks [10]. To compare like with like, we simulated trajectories and analyzed them by the same rules. We generated state transitions with the exact one-step transition matrix, accumulated displacement at the current velocity every 0.02 s, and sampled position at 2 frames s^{-1} for 30 s. We classified a whole track as stationary when its mean absolute frame velocity (the absolute displacement between consecutive frames divided by the frame interval) fell below 0.1 μm s^{-1}. For the remaining tracks, net velocities above +0.01 or below −0.01 μm s^{-1} defined anterograde and retrograde tracks, respectively. Because the first threshold uses speed, not net velocity, a vesicle that reverses can count as moving even if it finishes close to where it started. Moving tracks with net velocities inside the ±0.01 μm s^{-1} band were left out of the three whole-track proportions but were kept for the statistics pooled over moving tracks.

Within moving tracks, frame velocities above +0.1 or below −0.1 μm s^{-1} counted as anterograde and retrograde motion, respectively. Frames with velocities between these thresholds counted as pauses. We calculated the fraction of time in each class, pause and reversal frequencies, track length, and median segmental speed above the published cutoff (0.5 μm s^{-1} for APP and lysosomes, 0.1 μm s^{-1} for Rab5). The source study reported the Rab5 track length and pause frequency and the lysosome pause frequency for both directions combined. For these statistics, we pooled the simulated values from both directions before taking the median.

We digitized the summary statistics used as fitting targets from the published figures [10]. APP contributed 13 summaries, and lysosomes contributed 12. Because the three fractions in each classification sum to one, these provide at most 11 and 10 independent constraints, respectively. Rab5 contributed eight summaries and at most seven independent constraints. Whole-track classes were unavailable for that cargo.

2.3 Estimating rates from trajectory summaries

For each cargo and condition, we chose speeds, occupancies, and forward rates to minimize F, the sum of squared relative residuals. A relative residual is the difference between the simulated and measured values of a statistic, divided by the measured value. Some parameter sets leave a statistic undefined in the simulation; for example, the median segmental speed has no value when no simulated frame velocity exceeds the cutoff. We then set that relative residual to one, which is the penalty for a 100% error, so that a parameter set could not score better by failing to produce a target. A random search supplied starting points for repeated Nelder–Mead refinements [16]. Each evaluation simulated 1500

trajectories with the same random numbers, which keeps the objective from fluctuating between evaluations. We then rescored the candidates on a separate set of 20,000 trajectories and retained the candidate with the lowest score. Because the published summaries are derived from the same observations and their covariance is unknown, each fit gives a representative parameter set, and other combinations of rates may fit equally well.

To ask how many immobile states the observations can distinguish, we repeated the fit with three states (A, R, and P, with six parameters) and four effective states (A, R, P, and S, with eight parameters). In the four-state model, D serves only as a passage between P and S. For an assumed relative error σ per target, we used $\chi^2 = F/\sigma^2$ and two descriptive scores based on the Akaike information criterion (AIC) and the Bayesian information criterion (BIC). We calculated AIC = $\chi^2 + 2m$ and BIC = $\chi^2 + m \ln n$. Here, m counts fitted parameters and n counts targets after accounting for the sum-to-one constraints. We used σ = 0.10 and 0.15. The latter approximates the spread of wild-type APP track classes across four recordings [10]. These scores weigh goodness of fit against the number of parameters under the stated error assumptions, and a lower score is better. Because the covariance among summaries is unknown, the scores are descriptive and are not formal statistical tests.

We also tested sensitivity to errors in the digitized targets. Each target was multiplied by $\exp(0.1z)$, where z is a standard normal deviate, which perturbs each target by about 10%. For each APP and lysosome condition, we drew ten perturbed sets of targets, renormalized the proportions, and refitted the model to each set, starting from the adopted parameter vector. We call these the perturbation refits. The ranges reported below extend from the smallest to the largest values across the ten refits. In a separate check, we allowed speed to vary from run to run. At the start of each run, we multiplied the directional speed by a lognormal variate with unit mean and a fitted coefficient of variation.

2.4 How far a vesicle travels before turnover

The movies describe events over seconds. To predict where cargo accumulates over hours, we follow a population supplied from the soma as its vesicles switch states and are lost to turnover. Let a, r, p, d, and s be the steady-state linear densities (vesicles per unit length of axon) in the five states and λ their common first-order loss rate. Balancing transport, transitions, and loss for each state gives

$$\mathrm{d}(v_\mathrm{a}a)/\mathrm{d}x = -(k_\mathrm{ap} + \lambda)a + k_\mathrm{pa}p \tag{3}$$

$$-\mathrm{d}(v_\mathrm{r}r)/\mathrm{d}x = -(k_\mathrm{rp} + \lambda)r + k_\mathrm{pr}p \tag{4}$$

$$0 = k_\mathrm{ap}a + k_\mathrm{rp}r - (k_\mathrm{pa} + k_\mathrm{pr} + k_\mathrm{pd} + \lambda)p + k_\mathrm{dp}d \tag{5}$$

$$0 = k_\mathrm{pd}p - (k_\mathrm{dp} + k_\mathrm{ds} + \lambda)d + k_\mathrm{sd}s \tag{6}$$

$$0 = k_{ds}d - (k_{sd} + \lambda)s \tag{7}$$

Eliminating the three immobile-state densities leaves two exponential solutions, or modes. One decays away from the soma, and the other decays away from the terminal. For the fitted APP rates and boundary conditions tested, the terminal mode decays within about 10 μm of the terminal. In axons longer than 400 μm, varying terminal uptake, return, or distal supply therefore changes the profile in the imaged 0–200 μm segment by less than 0.1%. For this reason, we keep only the mode that decays away from the soma. Its total density $C = a + r + p + d + s$ falls as $\exp(-x/\ell)$, where ℓ, the attenuation length, is the distance over which density decreases by a factor of e. We used $\lambda = (\ln 2)/(3.63\ \text{h})$, corresponding to a half-life of 3.63 h estimated from a log-linear fit to optic-nerve APP decay (Table 1 of Ref. [17]), and repeated the calculation using the 2.5-h half-life measured for bulk APP in cortical neurons [18].

Turnover also changes the mix of states among the vesicles available for tracking. For example, Eq. (7) gives the long-lived stationary state a local density ratio $s/d = k_{ds}/(k_{sd} + \lambda)$, whereas the closed chain, which has no turnover, has the steady-state occupancy ratio $\pi_S/\pi_D = k_{ds}/k_{sd}$. We therefore initialized the simulated APP movies with the local state composition from Eqs. (3)–(7). The spatial and movie calculations then describe the same surviving population. Summing the five balances cancels all transitions between states and gives a balance for the net flux J,

$$\mathrm{d}J/\mathrm{d}x = -\lambda C, \quad J = v_a a - v_r r \tag{8}$$

For a single exponentially decaying population on a long axon, the net flux tends to zero far from the soma. Integrating Eq. (8) from the observation point outward then gives

$$J(x)/C(x) = \lambda\ell \tag{9}$$

Equation (9) makes the spatial prediction testable in a live axon, because its left side can be measured directly. At a fixed position, count the forward crossings per second, subtract the backward crossings, and divide by the number of particles per unit length, including stationary ones. This gives J/C, the net flux per unit density, which has units of velocity. Its value can differ from the closed-chain drift in Eq. (2) because turnover alters the local state composition.

2.5 What the fluorescent tag detects

The antibody used for imaging recognizes the tag, not APP itself. Intact APP in a vesicle and any fragment that retains the tag therefore contribute to the same intensity profile. We digitized the fluorescence profiles of wild-type APP tagged with green fluorescent protein (APPwt-GFP), Swedish APP tagged with turbo red fluorescent protein (APPswe-tRFP), and tau at 5-μm intervals from 0 to 200 μm. Each profile was normalized to its intensity in the soma. The published mean profiles (Fig. 2C of

Ref. [10]) cover 20 neurons in six biological replicates. We held out the two-color control, in which both tags were fused to wild-type APP (Fig. S4C of Ref. [10]), to test the fitted model. For APP variant g (wild type, g = w, or Swedish, g = s), the model allows fluorescence from both transported APP and a tag-bearing product,

$$f_g(x) = \kappa A(x)[(1 - \varphi_g)c_g(x) + \varphi_g \exp(-x/\ell_F)] \tag{10}$$

The first term follows the transported density c_g, normalized to one at the axon hillock, where the axon leaves the soma (x = 0). The second describes a tag-bearing product that spreads from the soma with attenuation length ℓ_F. Its share of the hillock signal is φ_g. Both terms share the scale factor κ, the ratio of hillock to soma intensity, and are multiplied by $A(x) = \tau(x)/\tau(0)$, the measured tau profile, which serves as an empirical correction for variations in axon thickness and in antibody staining along the axon.

Which fragments can carry the tag depends on where the tag sits. A C-terminal tag remains on a membrane-bound fragment after α- or β-secretase cleavage and can subsequently be released as part of a soluble intracellular fragment by γ-secretase cleavage [19,20]. The source study [10] specifies a C-terminal tag for the plasmids. The lentiviral constructs used for the fixed-cell images have similar names, but their tag position was not reported. To relate the product shares of the two APP variants, we used the observation that Swedish APP yields about 2.8 times as much C99, the fragment left by β-secretase, in neurons as wild-type APP, with similar levels of C83, the fragment left by α-secretase, and a wild-type C83:C99 ratio of about 3:1 [20]. We assumed that the odds of product fluorescence at the hillock, $\varphi_g/(1 - \varphi_g)$, scale with the combined abundance of the two fragments, so that

$$\varphi_s/(1 - \varphi_s) = \theta\varphi_w/(1 - \varphi_w), \quad \theta = (3 + 2.8)/(3 + 1) = 1.45 \tag{11}$$

We fitted κ, φ_w, and ℓ_F by least squares to the two APP profiles over 5–200 μm. Setting φ_g = 0 gives the prediction for transport alone. Varying θ tests how strongly the results depend on the assumed link between fragment abundance and tag signal. To predict the two-color wild-type control, we supplied its own tau profile and kept the fitted parameters fixed. The movies came from neurons expressing one APP variant, whereas the images came from neurons expressing both. Applying movie-derived kinetics to the images therefore assumes that each variant moves in the same way whether it is expressed alone or with the other (Sec. 4). Implementation details are given in the Appendix.

3 Results

3.1 Moving frames are common even when most tracks are stationary

Two published observations about Swedish APP seem at first to conflict. A viewer following a moving Swedish APP vesicle would see motion in three of every four frames. A viewer choosing from all

classified tracks would have a 78% chance of choosing a stationary one [10]. The two observations refer to different populations. The first describes how a moving vesicle spends its time. The second counts tracks classified as stationary over the whole recording. Applying both selection rules to the simulations recovered both observations (Table 2). When we instead treated the percentages as fractions of the same population, the residual roughly doubled. The moving tracks also revealed a change in directionality. The measured ratio of anterograde to retrograde time fell from 1.46 for wild type to 1.00 for Swedish APP. The fits gave 1.43 and 0.98.

For APP and lysosomes, the fits required separate states for pauses within a track and for immobilization throughout a movie. We used the five-state chain for comparisons across cargoes and repeated the fits with fewer states as a check (Appendix). Root-mean-square (RMS) relative errors for wild-type and Swedish APP were 8.6% and 6.5%. For Rab5 without and with Swedish APP, they were 7.5% and 12.1%, and for lysosomes with wild-type and Swedish APP, they were 7.3% and 4.6% (Fig. 2, Tables 1 and 2). The largest APP error was a 22% overestimate of wild-type retrograde track length. Only the pooled Rab5 track length with Swedish APP missed its target by more than 25% (28% high).

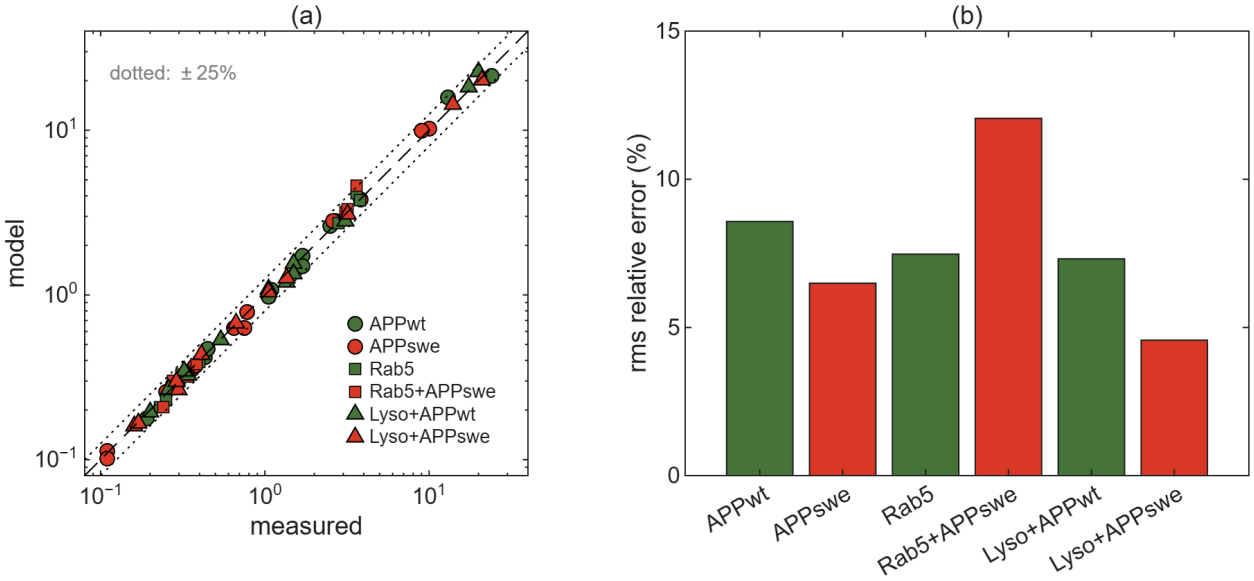


Fig. 2 Modeled and measured trajectory statistics for APP, Rab5 endosomes, and lysosomes under the six conditions in Table 1. Measurements are from the source study [10]. (a) All statistics; dotted lines mark ±25%. (b) Root-mean-square relative error for each condition.

Table 1 Fitted constants, steady-state occupancies, net drift, and fit error for each condition. Rates are in s^{-1}. The occupancies and drift refer to the closed chain [Eqs. (1a)–(1d) and (2)]. APP movie simulations instead start from the open-population composition (Sec. 2.4).

	APPwt	APPswe	Rab5	Rab5 + APPswe	Lyso + APPwt	Lyso + APPswe
v_a (μm s^{-1})	1.07	0.629	0.230	0.279	1.75	1.26
v_r (μm s^{-1})	1.75	0.630	0.208	0.209	1.35	2.18
k_{ap}	0.242	1.61	1.28	1.55	2.56	0.280
k_{pa}	0.625	1.13	1.05	2.93	0.871	0.111
k_{rp}	6.02	2.07	1.37	1.51	0.376	4.00
k_{pr}	5.36	1.37	1.61	3.70	0.205	0.841
k_{pd}	2.27	0.0109	1.0×10^{-3}	2.18	2.8×10^{-5}	0.121
k_{dp}	1.25	0.0124	0.0115	2.45	2.0×10^{-4}	7.18
k_{ds}	1.9×10^{-3}	3.9×10^{-3}	4.2×10^{-3}	1.0×10^{-3}	1.2×10^{-5}	7.9×10^{-4}
k_{sd}	1.0×10^{-3}	4.0×10^{-4}	8.5×10^{-4}	7.4×10^{-3}	8.0×10^{-7}	4.1×10^{-6}
π_A	0.264	0.059	0.235	0.297	0.086	0.082
π_R	0.091	0.056	0.333	0.386	0.137	0.043
π_P	0.102	0.084	0.284	0.157	0.252	0.206
π_D	0.185	0.074	0.025	0.140	0.034	0.003
π_S	0.357	0.727	0.122	0.019	0.492	0.665
v_{eff} (μm s^{-1})	+0.1238	+0.0018	−0.0155	+0.0022	−0.0347	+0.0091
RMS relative error (%)	8.6	6.5	7.5	12.1	7.3	4.6

Table 2 APP trajectory statistics: measured [10] and modeled. The fractions of tracks are computed over classified tracks. The fractions of time are computed over moving tracks and sum to one before rounding.

Statistic	APPwt, measured	APPwt, model	APPswe, measured	APPswe, model
Fraction of time moving anterogradely	0.430	0.420	0.375	0.368
Fraction of time moving retrogradely	0.295	0.293	0.375	0.374
Fraction of time paused	0.275	0.287	0.250	0.257
Fraction of tracks, anterograde	0.450	0.471	0.110	0.113
Fraction of tracks, stationary	0.360	0.351	0.780	0.785
Fraction of tracks, retrograde	0.190	0.178	0.110	0.102
Track length, anterograde (μm)	24.0	21.3	10.0	10.2
Track length, retrograde (μm)	13.0	15.9	9.0	9.9
Pause frequency, anterograde (per 10 s)	1.70	1.73	2.70	2.81
Pause frequency, retrograde (per 10 s)	2.50	2.64	2.60	2.81
Reversal frequency (per 10 s)	1.70	1.49	3.85	3.79
Segmental speed, anterograde (μm s^{-1})	1.10	1.07	0.65	0.63
Segmental speed, retrograde (μm s^{-1})	1.05	0.98	0.75	0.63
RMS relative error		8.6%		6.5%

3.2 Swedish APP vesicles lose the distance gained on anterograde runs

Wild-type APP poses a useful puzzle of its own. In the fit, its vesicles ran faster backward than forward (1.75 versus 1.07 μm s^{-1}), yet the population advanced (Fig. 3(a), Table 1). The reason is run length, not speed. An anterograde run covered 4.42 μm on average. A retrograde run averaged just 0.29 μm and lasted an estimated 0.17 s, less than the 0.5 s between frames. A frame that contains such a run therefore also contains part of a pause, and the speed measured over that frame is lower than the run speed. This is consistent with the lower measured median retrograde segmental speed of 1.05 μm s^{-1}. The

higher fitted retrograde speed persisted across all ten perturbation refits (1.55–1.79 versus 1.07–1.08 μm s^{-1}). Wild-type vesicles spent 2.90 times as long in the anterograde state as in the retrograde state.

The Swedish mutation largely erased that asymmetry (Fig. 3(c)). The fitted anterograde run shrank to 0.39 μm, close to the 0.30-μm retrograde run. In the model, a moving vesicle could still travel at 0.63 μm s^{-1} in either direction, but the anterograde-to-retrograde occupancy ratio fell to 1.05. The population also spent less time moving (occupancy 0.114 versus 0.355 for wild type) and more time in the stationary state (0.727 versus 0.357). Together, these changes reduced closed-chain drift from +0.124 to +0.002 μm s^{-1}. Across ten perturbation refits, anterograde runs shortened 9.0- to 12.9-fold, anterograde speed fell to 59–61% of the wild-type value, and motile occupancy fell 2.7- to 3.3-fold. Retrograde run length changed by at most 34%. Wild-type drift stayed positive (+0.106 to +0.133 μm s^{-1}). The Swedish estimates straddled zero (−0.001 to +0.003 μm s^{-1}).

The loss of forward bias is visible in the observations themselves, without any fitting. Weighting the reported segmental speeds by directional time fractions and by the moving-track fraction gives +0.105 μm s^{-1} for wild type and −0.008 μm s^{-1} for Swedish APP. These values are rough proxies for drift, because they are calculated from group summaries and not from individual tracks. In four additional wild-type recordings covering tag choice, plasmid expression, and microfluidic chambers, anterograde tracks outnumbered retrograde tracks by 18–26 percentage points. The Swedish recordings ranged from a 2-point anterograde excess in the plasmid experiment to a 14-point retrograde excess in the distal microfluidic recording (Fig. 3(b)) [10]. Weighting the plasmid track classes by their reported particle velocities gave +0.09 to +0.11 μm s^{-1} for wild type and −0.07 to −0.08 μm s^{-1} for Swedish APP. The wild-type forward bias persisted across recordings, whereas even the sign of the Swedish drift proxy depended on the recording.

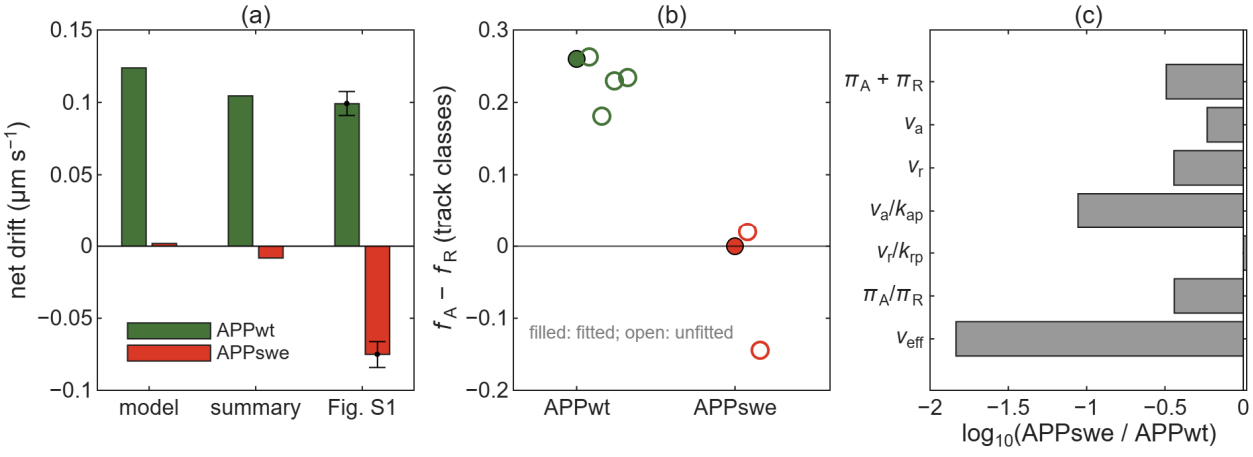


Fig. 3 Directional bias and estimated APP drift. (a) Net drift of APPwt and APPswe from the model [Eq. (2)], from the published summary statistics of the fitted recordings, and from unfitted plasmid recordings (Fig. S1 of Ref. [10];

bars span median-based and quartile-based velocity estimates). (b) Fraction of tracks classified as anterograde minus the fraction classified as retrograde in the fitted (filled) and unfitted (open) recordings of the source study [10]. (c) Ratio of model quantities, APPswe to APPwt, on a logarithmic scale.

3.3 The tracked vesicles account for too little distal fluorescence

With the same 3.63-h half-life for both variants, the modeled cargo density fell by a factor of e over 2385 μm for wild type and just 49 μm for Swedish APP. To compare this prediction with the images, we normalized each fluorescence profile to its own soma intensity and took the Swedish-to-wild-type ratio. In the first 100 μm, this ratio was predicted to be 0.47 and measured to be 0.96. In the next 100 μm, the prediction fell to 0.06, whereas the images still gave 0.79 (Fig. 4(a)).

Could a different half-life, again shared by both variants, reconcile the movies and images? No single value did. A 24-h half-life raised the distal ratio to 0.55, at the cost of an almost flat wild-type profile (attenuation length 15 mm). Shortening the half-life to 0.5 h brought the wild-type attenuation length to 365 μm, close to the 379 μm inferred from the uncorrected wild-type profile (Sec. 4), but drove the distal ratio to essentially zero. Uncertainty in the trajectory targets did not close the gap either. The perturbation refits gave Swedish attenuation lengths of 17–74 μm, and even the largest Swedish-to-wild-type distal ratio among them was only about 0.15.

We next kept the vesicle kinetics fixed and allowed a soma-derived product to carry part of the fluorescence signal [Eqs. (10) and (11), Fig. 4(b)]. The fitted product attenuation length was 531 μm. At $\theta = 1.45$, the model assigned the product 76% of wild-type and 82% of Swedish hillock fluorescence. The RMS error across the two profiles fell from 0.211 for transport alone to 0.041. The fitted and observed distal ratios were both 0.791. The proximal ratio was 0.896, compared with 0.964 observed. As an independent check, we then supplied the tau profile from the held-out two-color wild-type control. Without refitting, the RMS prediction error was 0.031, comparable to the 0.035 RMS difference between its two channels, both of which report wild-type APP (Fig. 4(c)). Omitting the tau correction raised the fit and control errors to 0.060 and 0.074. The result was insensitive to the assumed fragment ratio and half-life. The distal ratio remained between 0.786 and 0.793 as θ varied from 1 to 2.8 and reached 0.800 with a 2.5-h intact-APP half-life.

Which tagged species could spread this far? An attenuation length of 531 μm means that the product signal falls by only about 31% over the imaged 200 μm. APP diffusing in the plasma membrane spreads too slowly. The measured surface diffusivities for wild-type and Swedish APP are 0.041 and 0.007 $\mu m^2 s^{-1}$ [21]. Even with a surface half-life of about 19 h [18], spread along the membrane from the soma gives attenuation lengths of only 64 and 26 μm (the square root of the ratio of diffusivity to loss rate). A shorter-lived membrane fragment [20] with comparable diffusivity would not reach as far. A soluble

product is a more plausible candidate. A C-terminal tag can remain on a soluble intracellular fragment released by γ-secretase cleavage [20], and cleavage of C-terminally tagged Swedish APP produces diffuse cytoplasmic fluorescence [19]. Somatic processing contributes substantially to axonal APP products [22]. Some C-terminal fragments also travel in carriers distinct from those containing full-length APP [23], [24]. For a soluble product, assuming nearly complete APP cleavage [18], one tagged product per cleavage, and equal signal per molecule, the fitted share and attenuation length imply a product half-life of 8–12 h and a diffusivity of 5–7 $\mu m^2\ s^{-1}$.

The profiles show how far the label reaches but say much less about what it is. Several alternatives fitted almost equally well. Allowing local formation of the product in proportion to the loss of intact APP gave errors of 0.0409, 0.0408, and 0.0411 at conversion yields of 0, 0.2, and 0.5. Complete local conversion gave an error of 0.0483. A model with two carrier populations also fitted the profiles (error 0.036). The movies constrain that alternative, however. The moving-track statistics limit the possible contribution of moving wild-type-like carriers to the Swedish population. The similar composition of proximal and distal moving tracks [10] also weighs against a slow carrier class that disappears with distance. Choosing among these possibilities requires an independent measurement that connects the observed intensity to the material actually moving along the axon (Fig. 4(d)).

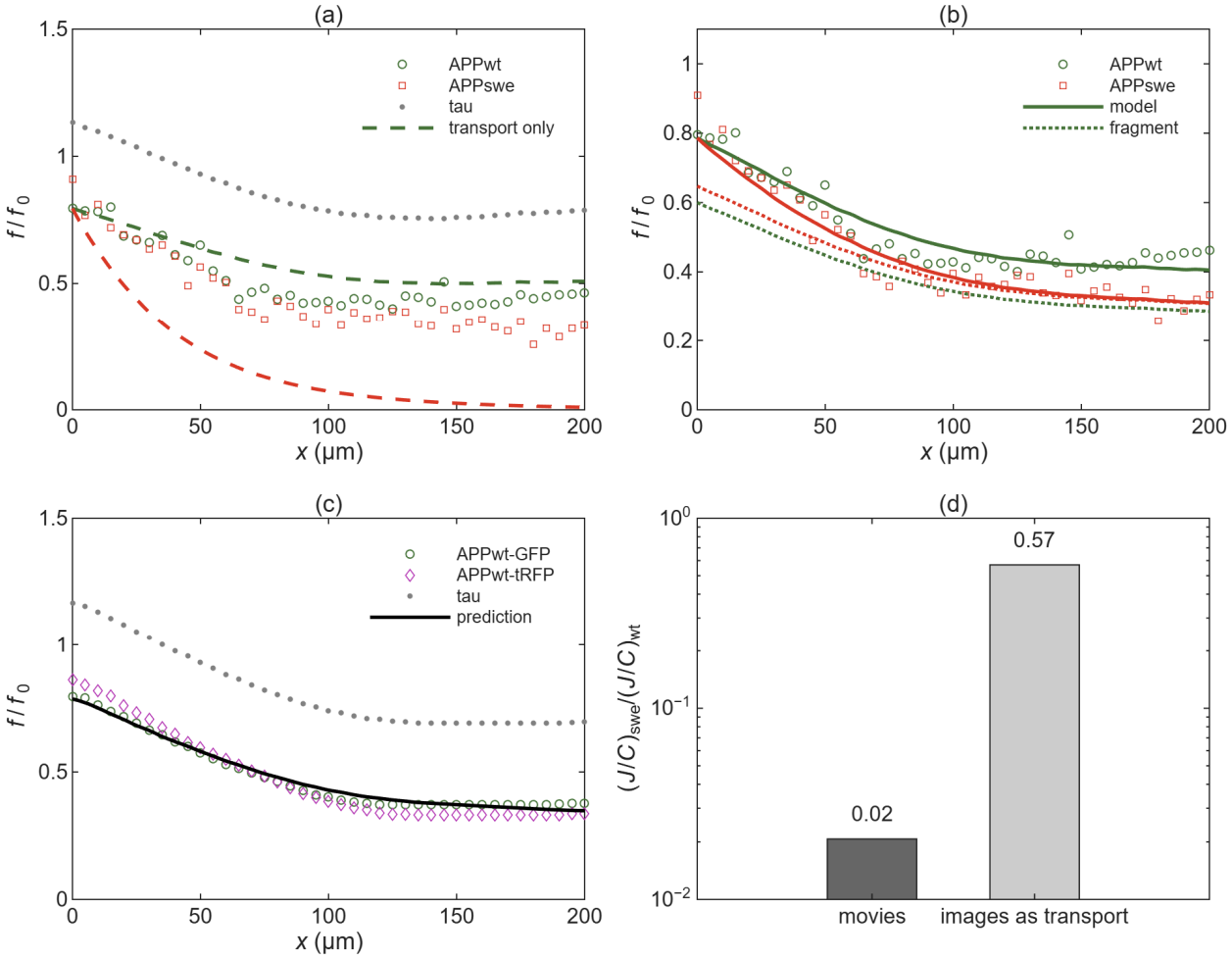


Fig. 4 Fluorescence profiles and model predictions. (a) Soma-normalized fluorescence of APPwt and APPswe and the tau profile in co-expressing axons, digitized from Fig. 2C of the source study [10], with the transport-only prediction (dashed). (b) The same data with the soma-derived product model, Eqs. (10) and (11) (solid); dotted lines show the product. (c) Two-color wild-type control (Fig. S4C of Ref. [10]) and the prediction of the model in (b) without refitting any parameters. (d) Swedish-to-wild-type ratio of the net flux per unit density, Eq. (9), predicted by the movie kinetics and required if the images were single-population transport profiles.

3.4 The fits predict more frequent and shorter retrograde lysosome runs

The recordings of other cargoes offer a test of why retrograde transport changes. In the source study, more dynactin, an activator of the retrograde motor dynein, was associated with Swedish APP even though total dynactin remained unchanged [10]. If Swedish APP draws activated dynein–dynactin [25] from a fixed, well-mixed pool shared by all cargoes, other cargoes should have fewer opportunities to start a retrograde run. We call this the fixed-pool hypothesis. In the model, we quantified those starts in two ways. The entry rate k_{pr} is the number of starts per unit time spent paused. Multiplying by the paused fraction gives $k_{pr}\pi_P$, the number of starts per particle per unit time. The two measures can change by different amounts when the time spent paused changes.

Lysosome fits gave the clearest test (Fig. 5), and the result was the opposite of what the fixed-pool hypothesis predicts. With Swedish APP, the fitted frequency of retrograde-run starts per lysosome rose 3.37-fold, while the mean distance per retrograde run fell from 3.58 to 0.54 μm. Because the runs were so much shorter, retrograde occupancy still fell from 0.137 to 0.043, and net drift shifted from −0.035 to +0.009 μm s^{-1}. The entry rate rose 4.11-fold. Both measures of initiation increased more than threefold in every candidate fit with an objective value no greater than 1.5 times the minimum. In ten paired perturbation refits, the frequency ratio was 2.5–5.4, the entry-rate ratio was 3.5–6.5, and the run-length ratio was 0.12–0.19. The preferred four-state fits likewise gave frequency and entry-rate ratios of 3.23 and 4.53.

Rab5 endosomes gave a less decisive test. Their fitted entry rate rose 2.30-fold (1.26–4.97 across near-optimal fits), and the three-, four-, and five-state chains all gave increases (1.30-, 2.13-, and 2.30-fold). The frequency per endosome rose 1.27-fold in the adopted fit, but its range across fits, 0.71–1.66, included both a decrease and an increase. Net Rab5 drift shifted from −0.016 to +0.002 μm s^{-1}. The model-based evidence against the fixed-pool hypothesis therefore comes chiefly from the predicted increase in starts per lysosome.

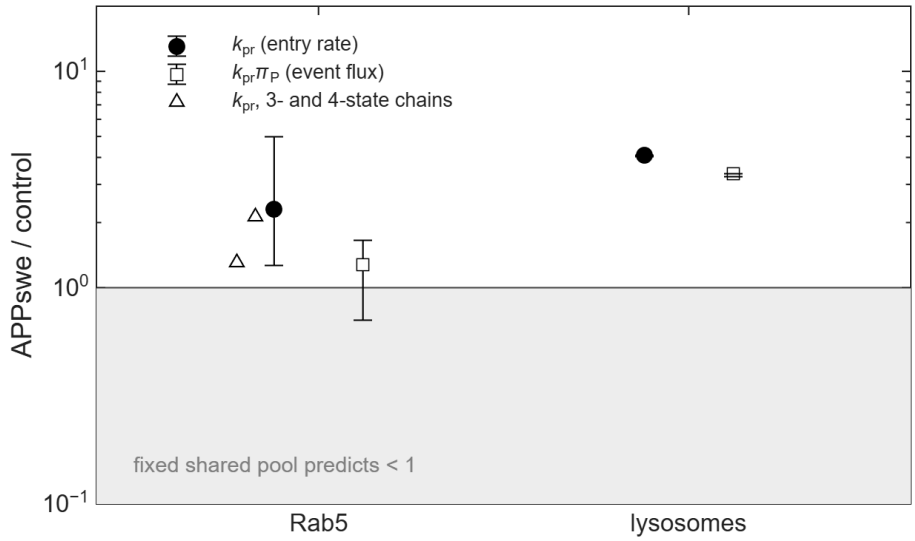


Fig. 5 Test of the fixed-pool hypothesis. Ratios of the APPswe condition to the control for the rate of entry into retrograde runs (k_{pr}, filled circles) and the event frequency ($k_{pr}\pi_P$, open squares) for Rab5 and lysosomes; bars span the ratios from all fits with an objective value no greater than 1.5 times the minimum, and triangles give k_{pr} for reduced three- and four-state Rab5 chains. The hypothesis predicts ratios below one (shaded).

4 Discussion

A bright distal axon would ordinarily be taken as a sign of efficient delivery of APP from the soma. Here, the short movies supply an independent estimate of how much signal that delivery could sustain.

Wild-type vesicles repeatedly gained several micrometers on an anterograde run and gave back only a fraction on a retrograde run. For Swedish APP, the two distances were nearly equal, and many tracks were classified as stationary throughout the recording. The source study interpreted the larger fraction of time that Swedish APP spent moving backward as evidence of enhanced dynein activation by dynactin. The fitted run lengths offer a second explanation. The fits reproduce the loss of net advance through shorter anterograde runs and less time spent moving, with retrograde run length nearly unchanged. A forward defect of this kind has precedents. Reduced kinesin activity has been associated with slower carriers and more reversals [26], and enhanced β-secretase processing impairs anterograde transport in mouse neurons [11]. The human data support a loss of persistent forward motion but leave the underlying motor interaction open.

Extrapolating from these movies to the images requires one further step. A short recording samples only vesicles that have survived long enough to reach the field of view, and their mix of states differs from that of the closed chain (Sec. 2.4). Initializing the simulation with this local population shortened the predicted wild-type attenuation length from 3620 to 2385 μm. Accounting for survival still left a large gap between predicted and observed distal Swedish fluorescence. The size of that gap gives an experiment a quantitative target.

The target is the Swedish-to-wild-type ratio of net flux per unit density. Under the stated transport and turnover assumptions, the movie kinetics and a reading of each image as a single transported population predict values of this ratio that differ by roughly a factor of 27 (Fig. 4(d)). For the movie kinetics, Eq. (9) gives J/C values of 0.127 and 0.0026 μm s^{-1} for wild-type and Swedish APP, respectively, a ratio of 0.021. If instead each image traces a single carrier population that decays exponentially with distance, the intensity in the distal 100-μm interval divided by that in the proximal interval equals $\exp(-100\ \mu m/\ell)$. The images then give attenuation lengths of 379 and 216 μm for wild-type and Swedish APP without the tau correction. With equal turnover rates, Eq. (9) gives a corresponding flux-per-density ratio of 216/379 = 0.57. Measuring genotype-specific turnover would allow this prediction to be adjusted if the rates differ.

These predictions can be tested by counting crossings at a fixed position along live axons (Table 3). Subtract backward crossings from forward crossings per second, then divide by the local number of particles per micrometer, including stationary particles. Compare that quantity between genotypes. A ratio near the movie prediction would indicate that net vesicle transport of Swedish APP is weak despite the distal signal. To identify what supplies the signal, verify the tag position, then assay tagged species in soluble and membrane fractions from the soma and axon. If a soluble fragment is present, its lifetime and axial spread can be checked against the fitted range.

Table 3 Model predictions and proposed tests for distinguishing transport from processing and for testing the fixed-pool hypothesis.

Prediction	Basis	Test
The predicted Swedish-to-wild-type ratio of net flux per unit density is 0.021 for the movie-based spatial model and 0.57 for a single population following the fluorescence profiles, assuming equal turnover rates.	Eq. (9) with the movie kinetics; Secs. 3.3 and 4; Fig. 4(d)	Count net directional crossings per second and particles per micrometer in the same registered segment of the same axons.
If the fitted long-range component is a soluble fragment, it accounts for about 76% of wild-type and 82% of Swedish APP tag intensity at the axon hillock.	Product model, Eqs. (10) and (11); Fig. 4(b)	Confirm the tag position in the constructs; immunoblot soluble and membrane fractions from the soma and axon with an anti-tag antibody.
Under the soluble-fragment interpretation, the fragment has a half-life of about 8–12 h and a diffusivity of about 5–7 $\mu m^2\ s^{-1}$.	Fitted ℓ_F and share, under unit-yield and equal-signal assumptions	Perform a pulse–chase experiment on the identified species; use local photoactivation to measure axial spread over time.
Swedish APP shortens mean anterograde runs about tenfold and reduces the motile fraction about threefold, while the mean retrograde run length remains similar.	Table 1; Fig. 3(c)	Measure the duration and displacement of individual runs in existing kymographs.
The fitted frequency of retrograde-run starts per lysosome is 3.37 times as high with APPswe as with APPwt.	Sec. 3.4; Fig. 5	Count retrograde-run starts per lysosome per second of recording. Dividing the number of starts by the time spent paused gives a separate estimate of the entry rate from the paused state.

Lysosomes provide a parallel test at the level of a single run. The source study reported weaker retrograde lysosome transport with Swedish APP. The fits attribute this to shorter runs, not fewer runs. Retrograde runs started more frequently per lysosome, yet covered less distance before stopping. Counting retrograde-run starts per lysosome per second of recording would therefore test the fixed-pool hypothesis directly, because the hypothesis predicts fewer starts with Swedish APP. An increase in starts would argue against a fixed pool and would motivate examining how cells regulate motor recruitment and run duration separately.

The conclusions about motors are limited by what the published trajectory summaries contain. They lack individual track durations, axon and replicate identifiers, and covariances. The ten perturbation refits quantify sensitivity to assumed errors in the targets, not biological variability. Estimating biological uncertainty would require raw tracks and a likelihood that accounts for runs and pauses truncated by the end of a movie or by the loss of a particle. Several immobile-state rates remain weakly constrained. The five-state chain has ten free parameters, set against at most 11 independent constraints for APP, 10 for lysosomes, and 7 for Rab5. The close fits in Fig. 2 therefore show that the chain can reproduce the summaries, not that its rates are unique.

A second limitation arises at the scale of a frame. In 9 of 12 directional comparisons, the observed median segmental speed exceeded the fitted run speed. Raising the fitted run speeds would not help, because the model already overestimates path length. For Rab5, modeled speeds were 8–13% low and

pooled track lengths 15–28% high. For retrograde APP, the corresponding discrepancies were 7–16% and 10–22%. Allowing run speeds to vary between runs with a lognormal distribution did little to help. At a fixed mean, a broader lognormal distribution lowers the median, and a frame that spans a pause or reversal averages over it. For wild-type anterograde APP, the simulated median fell from 1.07 to 1.00 μm s^{-1} at a coefficient of variation of 0.3. Five of the six conditions gave fitted coefficients of just 0.04–0.05. Penalized scores rose (ΔAIC = +1.4 to +4.2 at $\sigma = 0.10$). Localization error could inflate apparent speed but would also lengthen paths. Raw tracks would make it possible to test whether the tracking software joined detections from different vesicles into one track or split the trajectory of one vesicle into several shorter tracks.

The biochemical interpretation depends especially on which end of APP bears the tag in the lentiviral construct. An N-terminal tag would remain on the secreted ectodomain after α- or β-secretase cleavage. A soluble intracellular product requires a C-terminal tag. The movies and the images also came from different preparations. Each movie was recorded in neurons expressing one APP variant, whereas the images came from neurons co-expressing both. If the two variants share carriers, Swedish APP in a co-expressing axon need not move with the kinetics measured for it alone. The spatial estimates also depend on APP turnover measured in other preparations and on tau as an empirical correction for variations in axon thickness and in antibody staining along the axon. They assume a single loss rate for all five states. Because the fitted closed-chain occupancies of the stationary state S are 73% for Swedish APP and 36% for wild type, a state-dependent loss rate would change the two attenuation lengths unequally. The control profile tests the spatial prediction with the tau correction. It does not resolve the possible effects of co-expression or state-dependent turnover. Determining the identity of the labeled species still requires a molecular assay.

5 Conclusions

The fitted Swedish APP run lengths explain how appreciable motion can yield little net advance: anterograde runs became almost as short as retrograde runs. With the same 3.63-h half-life for both variants, the predicted Swedish-to-wild-type distal fluorescence ratio was 0.06, compared with 0.79 measured after soma normalization. A tagged product or second carrier population could account for the difference. This inference assumes that kinetics measured in neurons expressing one variant apply in neurons expressing both and that loss rates are equal across genotypes and states. Lysosome fits predicted more frequent but shorter retrograde runs, which argues against sequestration from a fixed pool of activated motors. Counting particle crossings and identifying tagged species in the same region would test these interpretations.

Appendix

Numerical implementation

We used base MATLAB R2026a (The MathWorks, Natick, MA), advancing the state of each vesicle with the transition matrix $\exp(Q\Delta t)$, where Q is the generator of the five-state chain and $\Delta t = 0.02$ s. A Mersenne Twister supplied random numbers. Reusing the seed made F deterministic during Nelder–Mead optimization. We optimized the logarithms of the two speeds, five occupancies, and four forward rates, renormalized the occupancies to sum to one, and calculated the reverse rates by detailed balance.

Each refinement used two simplex searches of up to 1500 evaluations each, with tolerances of 10^{-4} on the parameters and 10^{-5} on F. After the random search, we repeated refinement from the best vector and six perturbed copies, adding normal deviates with standard deviation 0.3 to the log-transformed variables. We used a different seed for the 20,000 rescoring trajectories.

Eliminating p, d, and s from Eqs. (3)–(7) leaves a two-by-two linear system for a and r. Its eigenvalues and eigenvectors give exact exponential profiles without spatial discretization. We evaluated the profiles on a 0.5-μm grid and integrated the proximal and distal areas by the trapezoidal rule. We fitted Eq. (10) by Nelder–Mead from four starting points, using a logistic transform for the shares and logarithms for κ and ℓ_F. Refitting all six conditions takes several hours. Other calculations take about a minute.

How many immobile states the data resolve

APP and lysosome fits required separate states for brief pauses and for immobilization throughout a movie. A three-state chain with just one immobile state gave residual sums ranging from 1.8 to 26, compared with 0.03–0.10 for the five-state fits. Evidence for an additional intermediate arrest was cargo-dependent. At $\sigma = 0.10$, the five-state score was lower than the four-state score for wild-type APP (ΔAIC = 146). Four states gave the lowest scores for Swedish APP and both lysosome conditions (the five-state scores were higher by 2.5–3.5). Three states gave the lowest descriptive scores for Rab5, which had at most seven independent constraints (the five-state scores were higher by 8.0 and 4.5). The ordering was the same when we used BIC and when we set $\sigma = 0.15$.

Repeating the key comparisons with the preferred structure for each condition gave a Swedish APP drift of +0.002 μm s^{-1} and an attenuation length of 50 μm. The corresponding retrograde-entry ratios were 1.30 for Rab5 and 4.53 for lysosomes.

Nomenclature

$A(x)$ = tau intensity normalized to its value at $x = 0$, $\tau(x)/\tau(0)$; corrects for variations in axon thickness and in antibody staining along the axon
a, r, p, d, s = linear densities of cargo in states A, R, P, D, S
C = total density of transported cargo
c_g = normalized transport profile of APP variant g (g = w, wild type; g = s, Swedish)
F = sum of squared relative residuals minimized in the fit
f_g = soma-normalized fluorescence of APP variant g
J = net axial flux of cargo
k_{ij} = rate of transition from state i to state j, s^{-1}
m = number of fitted parameters
n = number of independent fitting targets
v_a, v_r = anterograde and retrograde run speeds, μm s^{-1}
v_{eff} = net drift, μm s^{-1}
x = distance from the soma, μm
z = standard normal deviate
θ = Swedish-to-wild-type product multiplier
κ = hillock-to-soma intensity ratio
λ = loss (turnover) rate of cargo, s^{-1}
ℓ = attenuation length of the transported cargo, μm
ℓ_F = attenuation length of the tag-bearing product, μm
π_i = steady-state occupancy of state i
σ = assumed relative error per fitting target
τ = tau fluorescence intensity
φ_g = share of the hillock signal of APP variant g that comes from the tag-bearing product
χ^2 = error-weighted misfit, F/σ^2

Data Availability Statement

All experimental data analyzed in this study were taken from the source study [10] and its Supporting Information. The MATLAB code, the digitized data, and the fitted parameter sets that support the findings of this article are openly available on Zenodo [27].

References

[1] Koo, E. H., Sisodia, S. S., Archer, D. R., Martin, L. J., Weidemann, A., Beyreuther, K., Fischer, P., Masters, C. L., and Price, D. L., 1990, "Precursor of Amyloid Protein in Alzheimer Disease Undergoes Fast Anterograde Axonal Transport," Proc Natl Acad Sci U S A, **87**(4), pp. 1561–1565. https://doi.org/10.1073/pnas.87.4.1561.

[2] Kamal, A., Stokin, G. B., Yang, Z. H., Xia, C. H., and Goldstein, L. S. B., 2000, "Axonal Transport of Amyloid Precursor Protein Is Mediated by Direct Binding to the Kinesin Light Chain Subunit of Kinesin-I," Neuron, **28**(2), pp. 449–459. https://doi.org/10.1016/S0896-6273(00)00124-0.

[3] Stokin, G. B., Lillo, C., Falzone, T. L., Brusch, R. G., Rockenstein, E., Mount, S. L., Raman, R., Davies, P., Masliah, E., Williams, D. S., and Goldstein, L. S. B., 2005, "Axonopathy and Transport Deficits Early in the Pathogenesis of Alzheimer's Disease," Science, **307**(5713), pp. 1282–1288. https://doi.org/10.1126/science.1105681.

[4] Lazarov, O., Morfini, G. A., Pigino, G., Gadadhar, A., Chen, X., Robinson, J., Ho, H., Brady, S. T., and Sisodia, S. S., 2007, "Impairments in Fast Axonal Transport and Motor Neuron Deficits in Transgenic Mice Expressing Familial Alzheimer's Disease-Linked Mutant Presenilin 1," J Neurosci, **27**(26), pp. 7011–7020. https://doi.org/10.1523/JNEUROSCI.4272-06.2007.

[5] Welte, M. A., 2004, "Bidirectional Transport along Microtubules," Current Biology, **14**(13), pp. R525–R537. https://doi.org/10.1016/j.cub.2004.06.045.

[6] Hancock, W. O., 2014, "Bidirectional Cargo Transport: Moving beyond Tug of War," Nature Reviews Molecular Cell Biology, **15**(9), pp. 615–628. https://doi.org/10.1038/nrm3853.

[7] Maday, S., Twelvetrees, A. E., Moughamian, A. J., and Holzbaur, E. L. F., 2014, "Axonal Transport: Cargo-Specific Mechanisms of Motility and Regulation," Neuron, **84**(2), pp. 292–309. https://doi.org/10.1016/j.neuron.2014.10.019.

[8] Citron, M., Oltersdorf, T., Haass, C., McConlogue, L., Hung, A. Y., Seubert, P., Vigo-Pelfrey, C., Lieberburg, I., and Selkoe, D. J., 1992, "Mutation of the β-Amyloid Precursor Protein in Familial Alzheimer's Disease Increases β-Protein Production," Nature, **360**(6405), pp. 672–674. https://doi.org/10.1038/360672a0.

[9] Mullan, M., Crawford, F., Axelman, K., Houlden, H., Lilius, L., Winblad, B., and Lannfelt, L., 1992, "A Pathogenic Mutation for Probable Alzheimer's Disease in the APP Gene at the N-Terminus of β-Amyloid," Nat Genet, **1**(5), pp. 345–347. https://doi.org/10.1038/ng0892-345.

[10] Feole, M., Pozo Devoto, V. M., Dragišić, N., Arnaiz, C., Bianchelli, J., Texlová, K., Kovačovicova, K., Novotny, J. S., Havas, D., Falzone, T. L., and Stokin, G. B., 2024, "Swedish Alzheimer's Disease Variant Perturbs Activity of Retrograde Molecular Motors and Causes Widespread Derangement of Axonal Transport Pathways," J Biol Chem, **300**(4), p. 107137. https://doi.org/10.1016/j.jbc.2024.107137.

[11] Rodrigues, E. M., Weissmiller, A. M., and Goldstein, L. S. B., 2012, "Enhanced β-Secretase Processing Alters APP Axonal Transport and Leads to Axonal Defects," Hum Mol Genet, **21**(21), pp. 4587–4601. https://doi.org/10.1093/hmg/dds297.

[12] Reed, M. C., Venakides, S., and Blum, J. J., 1990, "Approximate Traveling Waves in Linear Reaction-Hyperbolic Equations," SIAM Journal on Applied Mathematics, **50**(1), pp. 167–180. https://doi.org/10.1137/0150011.

[13] Bressloff, P. C., and Newby, J. M., 2013, "Stochastic Models of Intracellular Transport," Reviews of Modern Physics, **85**(1), pp. 135–196. https://doi.org/10.1103/RevModPhys.85.135.
[14] Kuznetsov, I. A., and Kuznetsov, A. V., 2015, "A Coupled Model of Fast Axonal Transport of Organelles and Slow Axonal Transport of Tau Protein," Comput Methods Biomech Biomed Engin, **18**(13), pp. 1485–1494. https://doi.org/10.1080/10255842.2014.920830.
[15] Kuznetsov, I. A., and Kuznetsov, A. V., 2020, "Modeling Tau Transport in the Axon Initial Segment," Mathematical biosciences, **329**, p. 108468. https://doi.org/10.1016/j.mbs.2020.108468.
[16] Nelder, J. A., and Mead, R., 1965, "A Simplex Method for Function Minimization," The Computer Journal, **7**(4), pp. 308–313. https://doi.org/10.1093/comjnl/7.4.308.
[17] Morin, P. J., Abraham, C. R., Amaratunga, A., Johnson, R. J., Huber, G., Sandell, J. H., and Fine, R. E., 1993, "Amyloid Precursor Protein Is Synthesized by Retinal Ganglion Cells, Rapidly Transported to the Optic Nerve Plasma Membrane and Nerve Terminals, and Metabolized," J Neurochem, **61**(2), pp. 464–473. https://doi.org/10.1111/j.1471-4159.1993.tb02147.x.
[18] Moghekar, A., Rao, S., Li, M., Ruben, D., Mammen, A., Tang, X., and O'Brien, R. J., 2011, "Large Quantities of Aβ Peptide Are Constitutively Released during Amyloid Precursor Protein Metabolism in Vivo and in Vitro," Journal of biological chemistry, **286**(18), pp. 15989–15997. https://doi.org/10.1074/jbc.M110.191262.
[19] Tam, J. H. K., Seah, C., and Pasternak, S. H., 2014, "The Amyloid Precursor Protein Is Rapidly Transported from the Golgi Apparatus to the Lysosome and Where It Is Processed into Beta-Amyloid," Mol Brain, **7**, p. 54. https://doi.org/10.1186/s13041-014-0054-1.
[20] Wang, J., Gleeson, P. A., and Fourriere, L., 2024, "Spatial-Temporal Mapping Reveals the Golgi as the Major Processing Site for the Pathogenic Swedish APP Mutation: Familial APP Mutant Shifts the Major APP Processing Site," Traffic, **25**(3), p. e12932. https://doi.org/10.1111/tra.12932.
[21] Belapurkar, V., Mahadeva Swamy, H. S., Singh, N., Kedia, S., Setty, S. R. G., Jose, M., and Nair, D., 2023, "Real-Time Heterogeneity of Supramolecular Assembly of Amyloid Precursor Protein Is Modulated by an Endocytic Risk Factor PICALM," Cell Mol Life Sci, **80**(10), p. 295. https://doi.org/10.1007/s00018-023-04939-w.
[22] Niederst, E. D., Reyna, S. M., and Goldstein, L. S. B., 2015, "Axonal Amyloid Precursor Protein and Its Fragments Undergo Somatodendritic Endocytosis and Processing," Molecular biology of the cell, **26**(2), pp. 205–217. https://doi.org/10.1091/mbc.E14-06-1049.
[23] Muresan, V., Varvel, N. H., Lamb, B. T., and Muresan, Z., 2009, "The Cleavage Products of Amyloid-β Precursor Protein Are Sorted to Distinct Carrier Vesicles That Are Independently Transported within Neurites," J Neurosci, **29**(11), pp. 3565–3578. https://doi.org/10.1523/JNEUROSCI.2558-08.2009.
[24] Villegas, C., Muresan, V., and Ladescu Muresan, Z., 2014, "Dual-Tagged Amyloid-β Precursor Protein Reveals Distinct Transport Pathways of Its N- and C-Terminal Fragments," Hum Mol Genet, **23**(6), pp. 1631–1643. https://doi.org/10.1093/hmg/ddt555.
[25] McKenney, R. J., Huynh, W., Tanenbaum, M. E., Bhabha, G., and Vale, R. D., 2014, "Activation of Cytoplasmic Dynein Motility by Dynactin-Cargo Adapter Complexes," Science, **345**(6194), pp. 337–341. https://doi.org/10.1126/science.1254198.

[26] Kaether, C., Skehel, P., and Dotti, C. G., 2000, "Axonal Membrane Proteins Are Transported in Distinct Carriers: A Two-Color Video Microscopy Study in Cultured Hippocampal Neurons," Mol Biol Cell, **11**(4), pp. 1213–1224. https://doi.org/10.1091/mbc.11.4.1213.
[27] Kuznetsov, A. V., 2026, "MATLAB Code for 'Moving Without Making Progress: Shorter Forward Runs Explain the Loss of Net Advance in a Model of Swedish Mutant Amyloid Precursor Protein Transport.'" https://doi.org/10.5281/ZENODO.24200516.